JGR Space Physics

RESEARCH ARTICLE
10.1029/2019JA027713

Observations of Electron Precipitation During Pulsating Aurora and Its Chemical Impact

Fasil Tesema[1,2], **Noora Partamies**[1,2], **H. Nesse Tyssøy**[2], **Antti Kero**[3], and **C. Smith-Johnsen**[2]

[1]Department of Arctic Geophysics, The University Centre in Svalbard, Longyearbyen, Norway, [2]Birkeland Centre for Space Science, University of Bergen, Bergen, Norway, [3]Sodankylä Geophysical Observatory, University of Oulu, Oulu, Finland

Key Points:
- Spacecraft particle measurements were used to construct a statistical precipitation spectrum for 253 pulsating aurora events
- Large flux variations of energetic electron precipitation associated with pulsating aurora between the energies of 10 and 200 keV
- Model results showed mesospheric O_x destruction up to 78% for the median duration of pulsating aurora

Correspondence to:
F. Tesema,
fasil.tesema@unis.no

Citation:
Tesema, F., Partamies, N., Nesse Tyssøy, H., Kero, A., & Smith-Johnsen, C. (2020). Observations of electron precipitation during pulsating aurora and its chemical impact. *Journal of Geophysical Research: Space Physics*, *125*, e2019JA027713. https://doi.org/10.1029/2019JA027713

Received 11 DEC 2019
Accepted 24 APR 2020
Accepted article online 13 MAY 2020

Abstract Pulsating auroras (PsAs) are low-intensity diffuse aurora, which switch on and off with a quasiperiodic oscillation period from a few seconds to ~10 s. They are predominantly observed after magnetic midnight, during the recovery phase of substorms and at the equatorward boundary of the auroral oval. PsAs are caused by precipitating energetic electrons, which span a wide range of energies between tens and hundreds of keV. Such energetic PsA electrons will deposit their energy at mesospheric altitudes and induce atmospheric chemical changes. To examine the effects of energetic PsA electrons on the atmosphere, we first collect electron flux and energy measurements from low-latitude spacecraft to construct a typical energy spectrum of precipitating electrons during PsA. Among the 840 PsA events identified using ground-based auroral all-sky camera (ASC) network over the Fennoscandian region, 253 events were observed by DMSP, POES, and FAST spacecraft over the common field of view of five ASCs. The combined measurements from these spacecraft enable us to obtain an energy spectrum consisting of nonrelativistic and relativistic (30 eV to 1,000 keV) electrons during PsA. The median spectrum was found to be in good agreement with earlier estimates of the PsA spectra. We then use the Sodankylä Ion-neutral Chemistry (SIC) model to assess the chemical effect of PsA electrons. The observed extreme and median spectra of PsA produce a significant depletion in the mesospheric odd oxygen concentration up to 78%.

1. Introduction

Pulsating auroras (PsAs) are characterized by their quasiperiodic low-intensity (few kilo Rayleigh at the green and blue line emissions) variations centered around 100 km altitude (McEwen et al., 1981; Stenbaek-Nielsen & Hallinan, 1979). The emission patches have a horizontal scale size ranging from 10 to 200 km, and they switch on and off with periods from a few to tens of seconds (Lessard, 2012; Royrvik & Davis, 1977; Yamamoto, 1988). The on-time period is shorter with higher energy precipitation (Dahlgren et al., 2017; McEwen et al., 1981) and shows relatively small variations from pulse to pulse compared to the off-time periods (Yamamoto, 1988). PsAs are composed of separate east-west elongated or irregularly shaped patches, which are usually pulsating out of phase from each other with a slightly different period (Sato et al., 2004; Yamamoto, 1988). They are frequently observed at the equatorward boundary of nightside auroral oval and during substorm recovery phases (Lessard, 2012; Nishimura et al., 2020). PsAs are also reported to occur before a substorm onset (McKay et al., 2018), in the premidnight sector during active times (Bland et al., 2019; Partamies et al., 2017), and can persist for up to 15 hr (Jones et al., 2013). They may appear simultaneously in both hemispheres with different shapes and pulsation periods (Sato et al., 2004).

Grono and Donovan (2018) reported three subcategories of PsA based on stability and spatial extent: patchy, amorphous, and patchy PsA. Patchy aurora consists of stable emission structures with pulsations of limited spatial area, patchy PsA is made of steady emission structure with pulsations over much of their spatial extent, and the amorphous type is unstable and rapidly varying PsA. Both patchy and patchy PsA follow magnetospheric convection and were suggested to be a convenient and accurate method to remote sense convection (Yang et al., 2015, 2017). However, amorphous PsA type is more dynamic and has no relation to the convection. Among the three categories the most dominant type is amorphous PsA followed by patchy and pulsating patchy aurora (Grono & Donovan, 2020). Patchy and patchy PsA are suggested to originate from inner magnetosphere, while the source of amorphous PsA can extend radially farthest out from the inner magnetosphere (Grono & Donovan, 2020).

Despite different structures, the mechanism behind the PsA is the precipitation of energetic electrons that originate from the modulation of magnetospheric electrons by wave-particle interactions (Fukizawa et al., 2018; Kasahara et al., 2018; Nishimura et al., 2010, 2011). The energy of the particles is on the order of keV to several tens of keV (Johnstone, 1978; Miyoshi, Oyama, et al., 2015; Sandahl et al., 1980; Sandahl, 1984). The dominant mechanism responsible for scattering magnetospheric electrons associated with precipitating PsA electrons is of much debate (Dahlgren et al., 2017; Mozer et al., 2018; Miyoshi, Saito, et al., 2015; Nishimura et al., 2018; Sato et al., 2004). Nishimura et al. (2010, 2011) provided direct evidence that lower-band chorus waves play a primary role in driving PsA. They further indicated that PsA can exist without upper-band chorus and electron cyclotron harmonic (ECH) waves. Recently, Kasahara et al. (2018) and Fukizawa et al. (2018) implemented the same combinations of measurements to show correlations between brightness fluctuations of the auroral patches with chorus and ECH waves, respectively.

A large range of precipitating electron energies have been measured during PsA. Sato et al. (2002) showed a one-to-one correspondence between optical PsA and the spatiotemporal variations of the downgoing electron fluxes >5 keV measured by Fast Auroral SnapshoT (FAST) spacecraft. Evans et al. (1987) reported a significant amplitude of fluctuation in the electron flux above 20 keV and smaller variations in those below 5 keV measured by National Oceanic and Atmospheric Administration (NOAA) 6 spacecraft overpassing PsA. Miyoshi, Saito, et al. (2015) discussed the energy spectrum of the precipitating PsA electrons generated by different magnetospheric wave sources. They showed that a stable electron precipitation at 1 keV is due to upper band chorus waves, while the lower band chorus waves control the electron precipitation with energies above 2 keV. Jaynes et al. (2013) also reported significant electron flux modulations between electron energies of 30 and 100 keV measured by Geostationary Operational Environmental spacecraft (GOES) 13 spacecraft. They further showed a high correlation between GOES 13 electron flux and PsA optical intensity. Samara et al. (2015) studied the energies of PsA electrons using overpasses of Reimei and Defense Meteorological spacecraft Program (DMSP) spacecraft during six PsA events. Their results showed that the energies causing PsA could range from 3 keV to 30 keV. Earlier rocket measurements of PsA showed that precipitating electrons have energies between 2 and 140 keV (McEwen et al., 1981; Sandahl, 1984; Whalen et al., 1971). A more recent study by Tsuchiya et al. (2018) found that PsA is associated with relativistic electron precipitation with energy range >100 keV using very low frequency (VLF) subionospheric radio wave propagation.

The electrons during PsAs can ionize neutral particles below 100 km (Miyoshi, Oyama, et al., 2015; Turunen et al., 2009, 2016). Electron density observations from the European incoherent scatter (EISCAT) radar have shown a D region (80–95 km) electron density enhancement during PsA events (Hosokawa & Ogawa, 2015). They reported electron density maximum altitude to be 10 km lower during the on-period compared to the off-period of PsA. Electron density enhancements below 70 km measured by EISCAT radar further suggest that the electron precipitation associated with PsA have energies up to hundreds of keV (Hosokawa & Ogawa, 2015; Miyoshi, Oyama, et al., 2015; Oyama et al., 2016; Turunen et al., 2016). Precipitation of PsA electrons can lead to significant production of odd hydrogen ($HO_x = H + OH + HO_2$) and odd nitrogen ($NO_x = N + NO + NO_2$) followed by catalytic reactions that destroy ozone in the polar mesosphere (Turunen et al., 2016).

However, the actual variation and range of the precipitation energy and flux related to PsA are not known. There is also no observational evidence of chemical changes during this type of precipitation. To fully understand the impact of energetic PsA electrons in the atmosphere, it is crucial to characterize the electrons spectra. Atmospheric models, such as Whole Atmosphere Community Climate Model (WACCM), use Kp and Ap indices to parameterize the energy input during energetic electrons precipitation (EEP) (Smith-Johnsen et al., 2018, and references therein); however, EEP associated with PsA often occurs during the recovery phase of a substorm, where magnetic deflection has already recovered. Thus, the use of magnetic indices may lead to an underestimation of the higher energy precipitation in to the atmosphere. In this paper, we will use an extensive data set from auroral all-sky cameras (ASCs) to detect PsA events together with in situ particle energy measurements to construct a typical precipitation energy spectrum with realistic variation. This is followed by investigation of chemical effects of the precipitating electrons by using the Sodankylä Ion-neutral Chemistry (SIC) model (Turunen et al., 2009; Verronen et al., 2005).

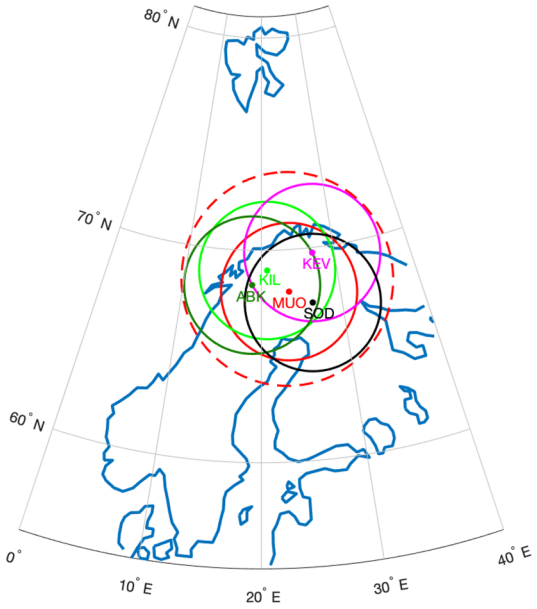

Figure 1. Geographic locations of ground based ASC stations in the Fennoscandian region from FMI-MIRACLE network. Color-coded circles around the stations show the full fields of view of the cameras. The red dashed circle, which comprises of all the ASC FOV, is the region where spacecraft overpasses are considered in the data analysis.

2. Data and Methods

The PsA events were identified by visual inspection of ASC keograms (Eather et al., 1976) from the MIRACLE network operated by the Finnish Meteorological Institute (FMI) (Sangalli et al., 2011). A keogram is a plot of north-south slices of individual ASC images, which are displayed as a function of time. We used data from Abisko (ABK, 68.36°N, 18.82°E), Kevo (KEV, 69.76°N, 27.01°E), Kilpisjärvi (KIL, 69.02°N, 20.87°E), Muonio (MUO, 68.02°N, 23.53°E), and Sodankylä (SOD, 67.42°N, 26.39°E) stations. For this study we extended the list by Partamies et al. (2017) to cover the years between 1997 and 2019. After all keograms were viewed, we searched for overpassing spacecraft that can measure precipitating electron energies. The region where the overpassing spacecraft are taken into consideration in the data analysis is the common field of view (FOV) of all the ASCs, which is indicated by the red dashed circle in Figure 1. A typical example of particle data from Polar Orbiting Environmental Spacecraft (POES) (from 0.189 keV to 1,000 keV) and DMSP (from 30 eV to 30 keV) is depicted in Figure 2c. From the 840 PsA events over the 23-year period of study, 253 events coincided with overpasses by DMSP (137), POES (240), and FAST (9) spacecraft with a total of 376 overpasses.

The electron and ion spectrometer analyzers on board FAST spacecraft are designed to measure energies of auroral particles with high pitch angle, temporal resolution, and sensitivity. They are used to obtain distributions of 48 energies at different angles with 1 s time resolution. The standard electron energy range measured by one of the analyzers is between 4 eV and 30 keV (Carlson et al., 1998). We analyze these data where the particles' pitch angle are below 3° to capture the precipitating population.

The special sensor for precipitating particles, Version 4 (SSJ4) and Version 5 (SSJ5) on board DMSP spacecraft is a particle spectrometer looking upward and designed to measure the flux of auroral electrons and ions with energies between 30 eV and 30 keV. Details about DMSP spacecraft SSJ measurements and data availability can be found in Redmon et al. (2017). We used the DMSP SSJ data archived in the Coupling Energetics and Dynamics of Atmospheric Regions (CEDAR) madrigal database.

The two sets of electron telescopes in the Medium Energy Proton and Electron Detector (MEPED) on board NOAA-POES spacecraft measure the flux of electrons which are pointing 0° and 90° with respect to local normal (Evans & Greer, 2000). At middle and high latitudes, the 0° telescope measures particle fluxes that will be lost to the atmosphere, whereas the 90° telescope might detect precipitating particle fluxes and/or trapped particles in the radiation belts (Rodger et al., 2010). As the level of pitch angle anisotropy varies significantly with particle energy, location, and geomagnetic activity, the 0° detector will underestimate,

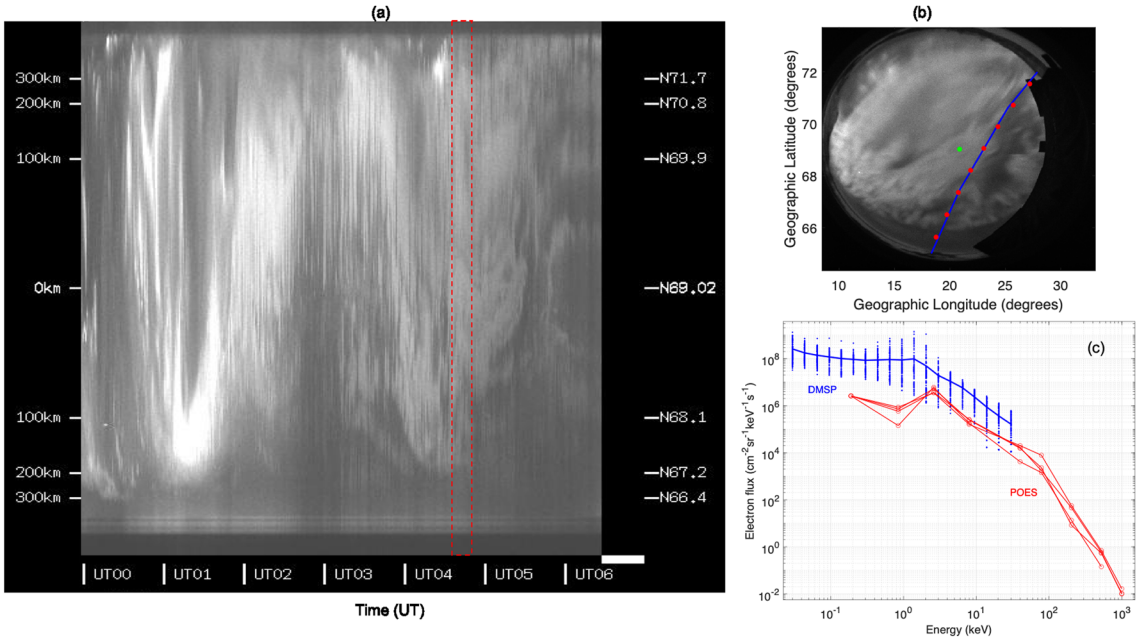

Figure 2. (a) Keogram generated from a series of KIL ASC camera images of green emission at 557.7 nm. (b) Overpasses of DMSP f16 (blue line, from 4:34 to 4:36 UT) with a time resolution of 1 s and NOAA-18 POES (red dots, 4:47 to 4:49 UT) with a time resolution of 16 s over Kilpisjärvi ASC image taken at 04:40 UT. The green dot shows the zenith of the ASC. (c) Spectrum constructed from the two spacecraft overpasses, on 22 January 2015. The red dashed box depicted on the keogram is the time between 4:34 and 4:49 UT, when both spacecraft were passing over KIL.

while the 90° detector will overestimate the flux of precipitating electrons. A more realistic estimate of the precipitating fluxes in the bounce loss cone can, however, be achieved by fitting the 0° and 90° fluxes onto the solution of the Fokker-Planck equation for particles (Nesse Tyssøy et al., 2016). The electron spectra are further corrected for low energy proton contamination, taking into account the degradation of the proton detectors. Cross contamination of relativistic electrons in the proton detector provides an extra electron energy channel. Finally, new optimized energy limits and associated geometric factors give the following four integral channels (>43, >114, >292, and >756 keV). Further details about the correction procedures and construction of optimized energy channels can be found in Nesse Tyssøy et al. (2016), Ødegaard et al. (2017), and Sandanger et al. (2015).

Total Electron Detector (TED) is another type of detector on board POES, which can measure low energy particle fluxes between 0.05 and 20 keV (Evans & Greer, 2000). POES-TED data are available as differential flux at four electron channels on both 0° and 30° telescopes with energy bands of 0.15–0.22, 0.69–1, 2.12–3.08, and 6.50–9.46 keV. In this study we use the 0° telescope measurement to account for the lower limit of electron precipitation. To construct the POES-MEPED differential flux from the integral flux measurements, we calculate the difference between consecutive energy channels. The centers of the channels are assumed to be the central energy. The data points obtained from this difference were fitted by a power law function (Whittaker et al., 2013), to derive the differential flux. This power law function was also used to extrapolate further points in both ends of the channels at 25 and 1,000 keV energies. With this approach we get nine data points at 0.19, 0.84, 2.60, 7.98, 25, 78.5, 203, 524, and 1,000 keV energies. To connect these data points, we use linear interpolation in a logarithmic scale.

To study the chemical effect of precipitating PsA electrons, we run the 1-D SIC model (Verronen et al., 2005) for the maximum, minimum, and average spectrum constructed from all overpasses. The SIC model is a coupled middle atmospheric ion and neutral chemistry model, which can be run in either steady state or time-dependent mode between 20 and 150 km altitudes with 1 km resolution. The model is known to capture ion and neutral changes in the atmosphere due to energetic particle precipitation (EPP) forcing (Verronen et al., 2016, and references therein). It includes hundreds of reactions consisting of 41 positive and 29 negative ions and 34 neutral species. It includes molecular and eddy diffusion but not atmospheric transport processes. The time-dependent mode is suitable for studying diurnal variations of atmospheric response due to external forcing such as electron and proton precipitations. We investigate effects due to

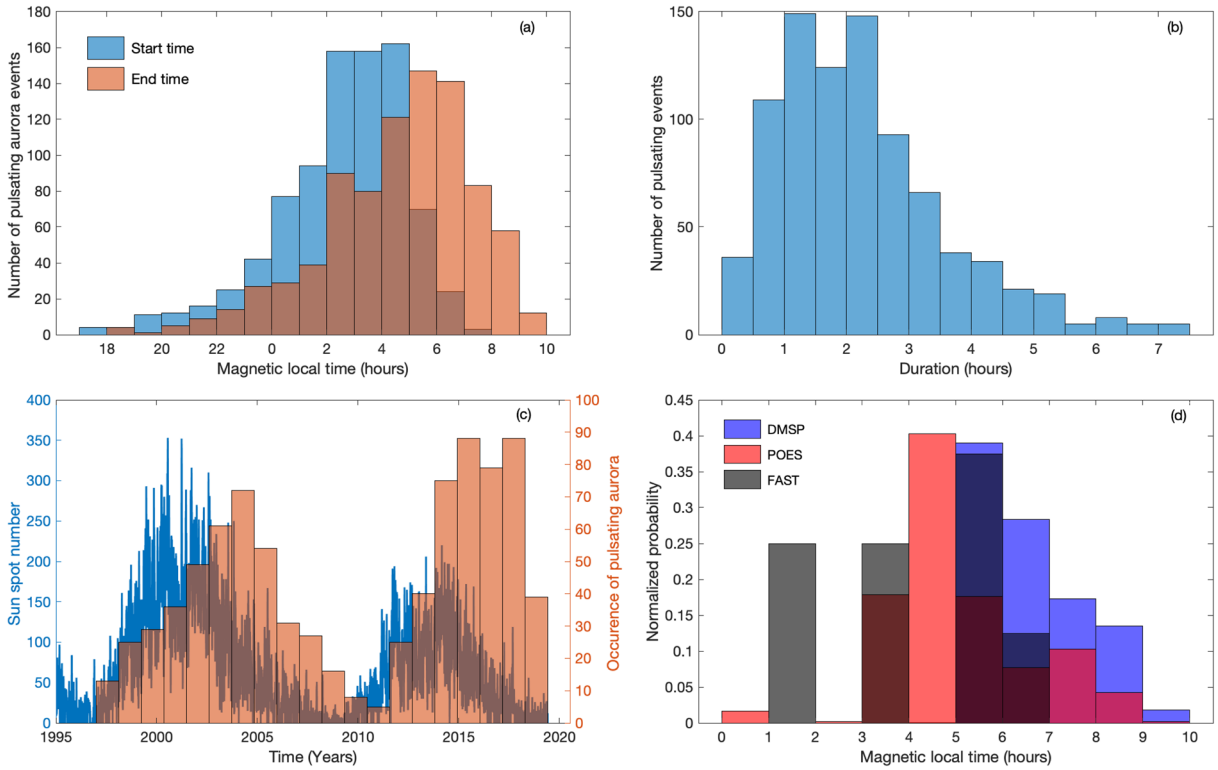

Figure 3. (a) A distribution of start and end times of all PsA events in MLT, (b) durations of the PsA events, (c) occurrence of PsA with respect to the sunspot number, and (d) self-normalized histogram of the MLT occurrence of spacecraft overpasses over the combined FOV of ASCs.

different durations and spectra of the PsA electrons forcing. More detailed explanation about the SIC model implementations is provided in Verronen et al. (2005) and Turunen et al. (2009).

3. Results

3.1. PsA Precipitation Energies

An analysis of precipitating electron measurements was undertaken using data from different spacecraft which are passing over PsA. Figure 2 shows an example of PsA ASC observation and electron spectra on 22 January 2015, during a moderate geomagnetic activity ($Kp = 3$). As it is shown in the keogram (Figure 2a), an active PsA that started just before 2 UT in the southern part of the FOV soon moved over the zenith. The PsA in the keogram is observed as consecutive bright and dark vertical stripes. The pulsation remains the dominant aurora type between 3:00 and 3:54 UT. It expanded southward and pulsated for nearly 20 min before retreating northward. The POES-NOAA18 spacecraft and DMSP-f16 spacecraft passed over the FOV at 4:47–4:49 and at 4:34–4:36 UT, respectively. The overpasses are shown in Figure 2b on the ASC image taken at 04:40 UT. The electron spectra during the overpasses are shown in Figure 2c. The solid blue line is the overpass average flux from DMSP, and the dots show the flux in one second time resolution during the overpass. The red curve shows the integrated measurements from POES-TED and MEPED instruments. From this figure, it can be seen that the electron flux between 700 eV and 2 keV, and between 10 keV and 30 keV show high variations. The softer precipitation of the energies between 3 and 10 keV undergo relatively small variations. POES TED and DMSP measurements show a large difference in the energy range below 2 keV. POES-MEPED measurements produce a smooth curve as a continuation of DMSP measurements toward higher energies.

As we used ASC data from five FMI-MIRACLE cameras, we could investigate some general characteristics of PsA events. In Figure 3a the distribution of the start and end times of the PsA events shows that these events are dominant during postmidnight to morning hours. The start time of the events peaks between 2:30 and 4:30 magnetic local time (MLT). The end time is a conservative estimate as many of the events were cut short due to the sunrise and the termination of imaging. The PsA events mostly end between 6 and 8 MLT.

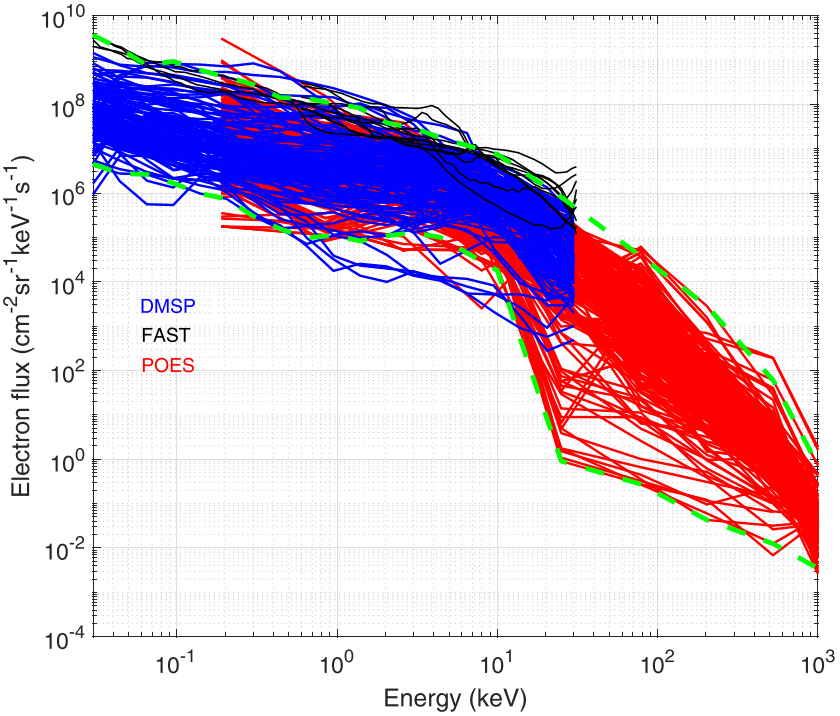

Figure 4. Constructed energy spectrum for pulsating aurora from a combination of 137 overpasses DMSP (blue), FAST 9 overpasses (black), and POES 240 overpasses (red), spacecraft measurements. The green dashed curves are the upper and lower boundaries of the spectra used in the SIC model run.

The duration of the events varies between 1 and 3 hr with a median value of 2 hr as shown in Figure 3b. There are also some events that persist longer than 4 hr. Figure 3c shows the annual number of PsA events with the sunspot number (SSN). The figure clearly shows a time shift of 1–3 years between the solar activity and the number of PsA events. Most of the events were observed during the declining phase of the solar activity. Comparing the two decline phases, the higher number of PsA events were found in the second one, where relatively low values of SSN in the whole solar cycle (2010–2019) were recorded.

Figure 4 shows all electron precipitation flux spectra from a combination of spacecraft overpasses over the common FOV illustrated in Figure 1. The electron fluxes are averaged over an overpass, while a spacecraft takes at most 4 min to cross the common ASC FOV. The spectra from different spacecraft (black, blue, and red colors for FAST, DMSP and POES, respectively) behave coherently at ~3 keV energy with small variation up to 10 keV. A considerable range of electron flux values with more than 2 orders of magnitude is evident with

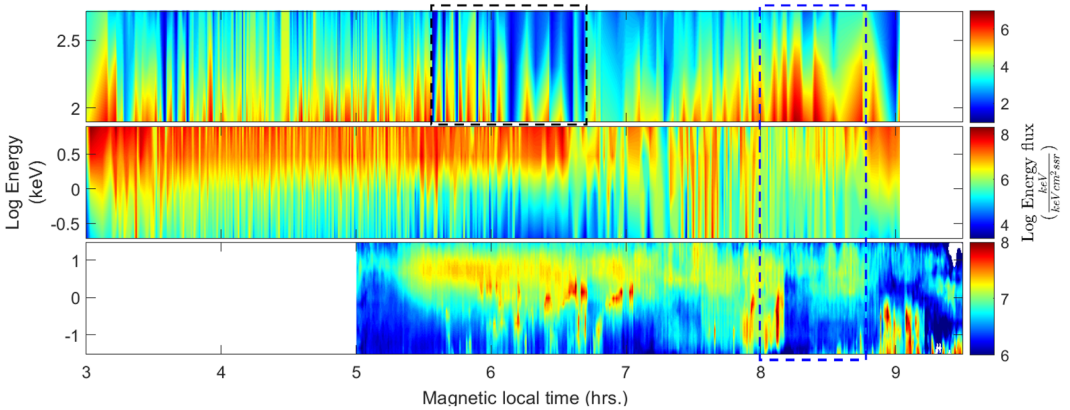

Figure 5. MLT evolution of PsA electrons energy spectra from MEPED and TED on board POES (upper two panels) and from DMSP (lowest panel) spacecraft.

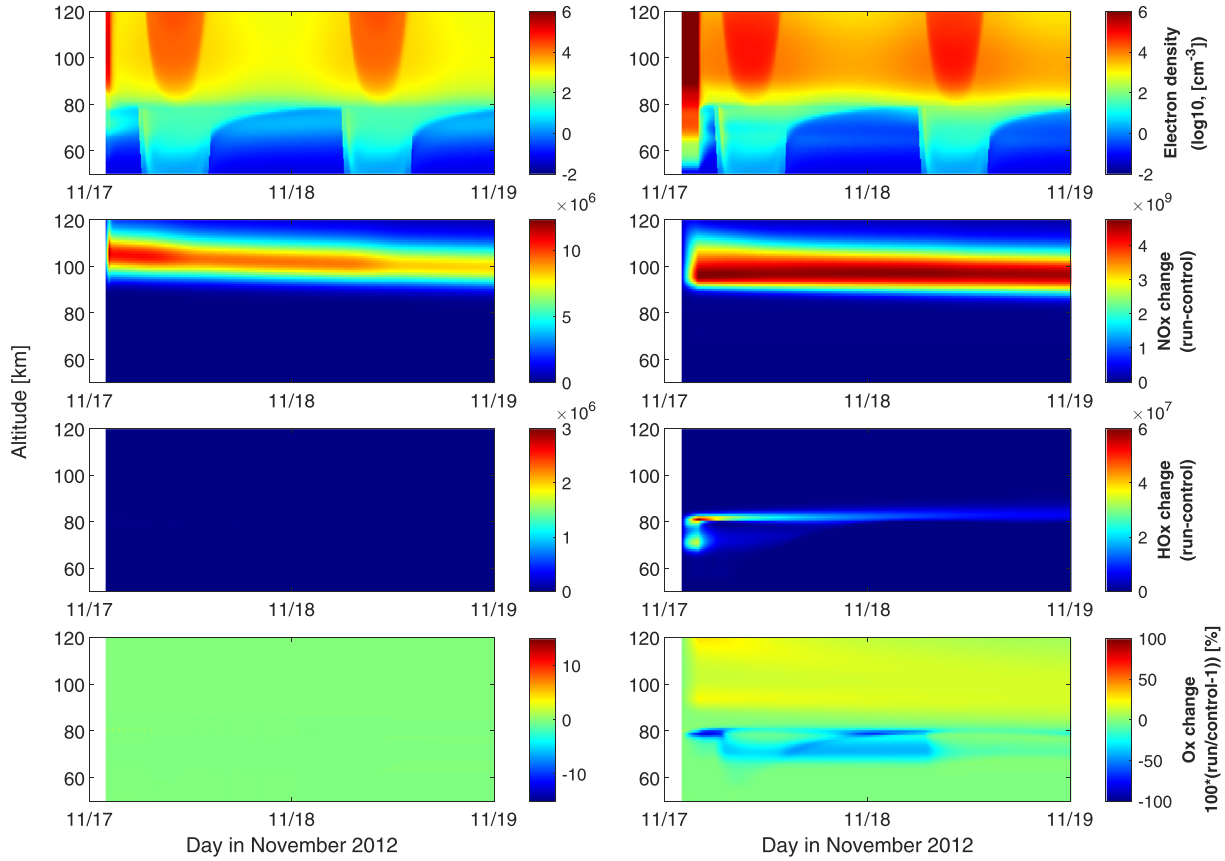

Figure 6. Modeled (from top), electron density (N_e), odd hydrogen (HO_x), odd nitrogen (NO_x), and odd oxygen (O_x). The left panels are forced with lower energy spectrum envelope from Figure 4 for 30 min, and the right panels are forced with the upper energy spectrum for 120 min. All model results are displayed for a 2-day time period.

the energies of <2 and >10 keV. Energies between 20 and 200 keV show the largest flux range. The overall spectrum shape is a smooth curve with significant variation in electron flux values in the high energy tail. For example, the flux at 30 and 100 keV ranges from 10^0 to 10^6 and 10^{-1} to $10^4 cm^{-2} keV^{-1} sr^{-1} s^{-1}$, respectively. The lowest spectra show a relatively sharp decrease at 10 keV. At the lower energy end of the spectrum, DMSP observations are coherent as compared to POES-TED measurements (red) at higher energies. Some of the differences seen can be due to the difference in MLT overpasses between the two spacecraft shown in Figure 3d. POES has a number of overpasses before 5 MLT, while all DMSP overpasses are after 5 MLT. The spectrum obtained from FAST spacecraft (black) lies at the upper boundary of all spectra and show sharp changes at energies higher than 20 keV. However, a large number of passes from DMSP and POES measurements together reflect smooth behavior.

By sorting all measurements from DMSP and POES spacecraft overpasses in time, we generate MLT evolution of the precipitating electrons energy flux spectra. We binned the energy flux of the precipitating electrons in 36 s time slots, which roughly accounts for on and off phases of PsA together (e.g., see Hosokawa & Ogawa, 2015), as shown in Figure 5. The first and second panels of Figure 5 are generated from POES-MEPED and POES-TED measurements, while the bottom panel consists of DMSP data. Generally, the MLT evolution of energetic particles from MEPED does not show any trend. However, there are abrupt decreases in flux around 5:30–6:30 MLT (dashed rectangle). Particles from TED with energies above 2 keV show high flux values until 6:30 MLT and a more systematic decrease in the morning hours passed 8 MLT. The third panel of Figure 5 shows relatively persistent fluxes at the electron energies between 1 and 10 keV over the entire period of observations. The prominent feature in this energy range is observed between 5:30 and 6:30 MLT, when the flux of ~10 keV electrons is nearly constant. Energy flux dropouts start to appear after 6:30 MLT. After 9 MLT, the harder precipitation starts to decay. The harder precipitation of electrons (>10 keV) shows a persistent value between 5:30 to 6:30 MLT followed by higher energy flux with dropouts,

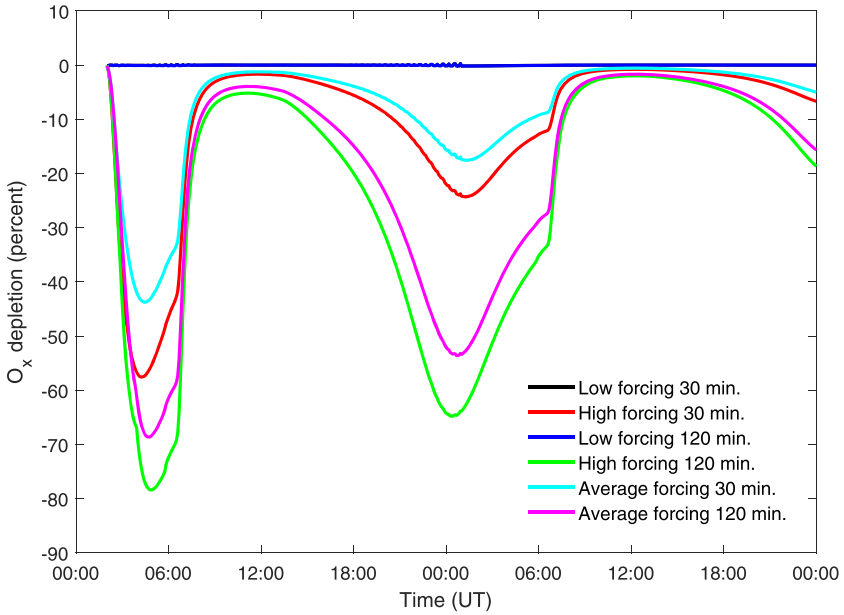

Figure 7. Relative differences in odd oxygen concentration at the maximum depletion altitude (79 km) with the different forcing durations for high, low, and average spectra. The modeled time span in 2 days.

particularly between 7 and 8:45 MLT. After 8:45, the flux at 10 keV energies are significantly reduced. The softer precipitation (<1 keV) shows a high variability throughout the whole observation period, with minima at 5 to 6, 7 to 7:30, and 8:10 to 8:50 and maxima values in the rest of the time period. The higher values of the softer precipitation are dominantly observed in the morning sector (after 7:30 MLT). Comparing the three panels of Figure 5, the precipitation lower than 10 keV decreases significantly after 6:30 MLT, while the higher energies either persist or show a tendency to increase in the morning sectors.

3.2. Atmospheric Effects of PsA

After initializing the SIC model at 68.02°N and 23.53°E (MUO station), the model run was performed for a randomly selected two day period on 17–19 November 2012 with and without the PsA forcing. The model temporal resolution was 5 min. We implemented the electron forcing for 30 and 120 min with the upper and lower boundaries of the spectrum, which are smooth curves identified by eye, as shown in Figure 4 (green dashed lines). By considering the median MLT of the spacecraft overpasses of to be at 4.5 MLT as shown in Figure 3d, the electron forcing was started at 2 UT (4.5 MLT in Fennoscandian sector) on 17 November 2012. The absolute and relative examined magnitudes of HO_x, NO_x, and O_x obtained from this model run are used to characterize the response of the atmosphere to the forcing. Figure 6 shows the model outputs of electron density, change in NO_x, change in HO_x, and percentage change in O_x with respect to the model run without forcing. The left panel shows a 30 min forcing with the lower boundary spectrum, and the right-hand side contains a 120 min forcing with the upper boundary spectrum. During the case of the shorter forcing, a significant enhancement of electron density reaches an altitude of 80 km. The NO_x response, in this case, was observed mainly between 100 and 120 km with the highest values at ~105 km at the time of forcing. The NO_x enhancement was centered around 100 km after 2 days with a value nearly half of the maximum. However, there were no observable HO_x and O_x changes. The case of the long time forcing with a harder spectrum showed an electron density enhancement at significantly lower altitudes reaching below 60 km. The NO_x change during this forcing was observed to be centered between 93 and 110 km with the maximum at 96 km. The change in HO_x shows a double maxima separated by ~10 km at the time of forcing. The largest HO_x change was observed at 81 km altitude with a value of 5.9×10^7 cm^{-3}, and the secondary maximum of 3.4×10^7 cm^{-3} occurred at 72 km. The primary increase in HO_x continued for more than 24 hr after the forcing. Consequently, the change in O_x showed the highest percentage depletion in a very narrow vertical extent at around 79 km until sunrise. After sunrise, a significant depletion persists as a double layer with the minimum values of −18% and −31% at altitudes of 81 and 71 km, respectively. The double structures observed during the daytime almost merged to create a vertically broader and more intense depletion during

the night. During the next day, the double layer depletion persisted but the magnitudes decreased to 7% and 17% at 72 and 79 km, respectively.

To study the temporal evolution of the change in O_x for the two days of the model run in more detail, we take the altitude of the maximum depletion observed during the entire model run time (79 km). In addition to the lower and upper boundary energy spectrum, we also calculated the average spectrum for the 30 and 120 min forcing as included in Figure 7. As mentioned above the atmosphere does not respond to the softer forcing scenarios. The four scenarios that showed significant depletions are from the averaged and upper boundary spectra. The maximum O_x depletion of these scenarios occurred 2.5 to 3 hr after the start of forcing. The average spectrum induced a maximum O_x depletion of 44% and 69%, and the upper boundary spectrum induce a depletion of 58% and 78% for 30 and 120 min forcing, respectively. The depletions in all these scenarios before sunrise showed a similar shape: a sharp decrease at the time forcing and a quick recovery before sunrise. However, the next day the change in O_x from these cases behaved differently. The O_x depletion during the longer forcing decreased quickly after sunset. The shorter forcing led to the maximum O_x depletion 25 min earlier on the forcing day and 40 min later in the following day compared to the longer forcing. The longer forcing induced almost the whole night of O_x depletion (>10%) even 24 hr after the forcing. The mesospheric O_x recovered during the next day, but the depletion continues during the night after. Comparing the maximum depletion between the day of forcing and the next day, the difference is smaller for the longer forcing. The O_x depletion is still significant (up to 20%) for the longer forcing after nearly 48 hr.

4. Discussions

We used an extensive data set of images and keograms from FMI-MIRACLE ASC network to identify 840 PsA events. In this study, the occurrence of PsA is highest from the local midnight until the end of the imaging in the morning sector. Our events have a median duration of 2 hr. The occurrence time is in a very good agreement with results from Grono and Donovan (2020). The PsA duration is also in agreement with previous statistical studies of PsA, which reported a duration between 1.4 and 2.25 hr (Bland et al., 2019; Jones et al., 2011; Partamies et al., 2017). PsA occurrence peaks toward the declining phase of the solar cycle. The declining phase of solar cycle is often associated with a high probability of high-speed solar wind streams and high occurrence frequency of EPP (Asikainen & Ruopsa, 2016), which is favorable for PsA.

Previous studies have indicated that the PsA electrons have energies between 2 and 200 keV. However, most of the studies have either been case studies or used an indirect method to obtain information about the precipitating PsA electrons energy (Miyoshi, Oyama, et al., 2015; McEwen et al., 1981; Sandahl, 1984; Sandahl et al., 1980; Whalen et al., 1971). This makes the results of such studies difficult to consider as representative for the typical energy range of precipitating PsA electrons. In this study, we used overpassing spacecraft to measure the PsA electrons during 253 events. We constructed PsA electrons energy flux spectra from different spacecraft measurements, which span energies between 30 eV and 1,000 keV with variable resolution. In Figure 4, it can be clearly seen that not all the spectra are smooth, but there are abrupt changes especially in connecting POES-TED and MEPED at energies from 20 to 80 keV, sudden increases in FAST observations above ~20 keV and sudden decreases in DMSP spectra above 10 keV. Keeping in mind that the MLT distribution shows fewer spacecraft overpasses in the morning sector (Figure 3d), Figure 5 (blue dashed rectangle) shows higher flux at higher energy range, while the softer precipitation decreases. Such increase in high energy flux in the late MLT sector was reported by Hosokawa and Ogawa (2015) and can be associated with a tendency to observe PsA in this sector. Furthermore, Hosokawa and Ogawa (2015) showed a higher electron density in late MLT PsA and the increase in the resonance energy of the pitch angle scattering in late MLT sector was suggested to be the cause for this increase in energy. Recently, Grono and Donovan (2018) categorized PsA into patchy, patchy pulsating, and amorphous PsA, Yang et al. (2019) further studied the energies of these categories and showed that one amorphous PsA case was related to energies centred around 20 keV, while a patchy PsA event had energies around 9 keV. The abrupt flux changes in the spectra could be related to a PsA subcategory change, which should be examined further in the future. It has been reported that different categories of PsA, patchy, patchy pulsating, and amorphous types, differ in time of occurrence, energy, and location (Grono & Donovan, 2020; Yang et al., 2019). Lacking harder precipitation between 5:30 and 6:30 MLT (Figure 5) but observing significant precipitation below 10 keV suggests that we are predominantly observing patchy PsA, which is associated with lower energy compared to amorphous

PsA. After 7 MLT softer precipitation decreases while harder precipitation tends to increase, which supports the dominance of the amorphous type PsA in the morning sector as reported by Grono and Donovan (2020).

As it is shown in the collection of spectra (Figure 4), the flux of PsA electrons in the medium energy (>30 keV) range is significant. Such energetic particles will strongly ionize the mesosphere and consequently destroy ozone through catalytic reactions involving HO_x (and NO_x) species (Sinnhuber et al., 2012, and references therein). This may further alter the thermal balance and the middle atmospheric dynamics. During winter this effect can propagate to lower altitudes and affect the lower stratospheric dynamics and regional climate over large timescales (Rozanov et al., 2012; Seppälä et al., 2013). Thus, the evaluation of the atmospheric response to PsA electron forcing was approached by using the SIC model with statistically characterized spectra. The absence of the atmospheric response to the forcing with a lower boundary spectrum raises the question on the threshold flux of energetic particles that can induce odd oxygen depletion. Forcing with the upper boundary spectrum indicated that the PsA electrons are capable of destroying a large amount of O_x species within a broad vertical extent (~10 km). A similar study by Turunen et al. (2016) showed strongest O_x depletion in the following day compared to the time of forcing. They reported mesospheric O_x depletion due to the electron forcing during a single PsA event to be between 14% and 82%. They discussed the possibility of an overestimation of the particle flux from the VanAllen probes' measurements and concluded the 25% depletion of odd oxygen to be realistic. The number of PsA events overpassed by the spacecraft represent 30% of all the events identified in this study. By taking the median duration of PsA (2 hr) as the duration of the forcing, together with the average spectrum, resulted in 69% depletion of O_x at the time of forcing and 54% during the following night. This is double the previously proposed ozone depletion.

Miyoshi, Oyama, et al. (2015) estimated the spectrum of a PsA event from EISCAT measurements. In their study, the spectra information from EISCAT electron density inversion was limited to energies below 100 keV. A reduced pitch angle scattering at relativistic energy range is suggested to lead to a high discrepancy between the estimated spectrum and spectrum measured by Van Allen Probes. Turunen et al. (2016) further investigate the uncertainity in the hard end of the spectrum using Metropolis-Hastings Markov chain Monte Carlo (MCMC) method. They conclude that the MCMC median spectrum, which lies between the estimated spectrum and Van Allen measurements spectrum is a reasonable one. This spectrum is in a very good agreement with our average spectrum, which further strengthens the significance of pitch angle scattering at relativistic energy range.

The O_x depletion of 44% we obtained soon after the forcing is significantly higher: (shown in Figure 6) compared to the 15% reported in Turunen et al. (2016). Because the highest energy end of the spectrum that predominantly affects the middle atmosphere was obtained from the POES spacecraft and the dominant overpassing time was between 4 and 5 MLT (1.5 to 2.5 UT, see Figure 3), we started the forcing at 2 UT. This is 2 hr earlier than in Turunen et al. (2016). Our results show that the magnitude of the depletion soon after the forcing is comparable to the depletion during the following night. This is not the case reported by the Turunen et al. (2016). They found a smaller depletion at the time of the forcing as compared to the following night for all the scenarios considered. The large O_x depletion shortly after the forcing suggests that a detectable mesospheric O_3 change could be measured in the future. Here, the average spectrum applied to the 30 min forcing resulted in 44% odd oxygen depletion, which is of the same magnitude as that during substrom electron precipitation (Seppälä et al., 2015). The short-term extremely large odd oxygen depletion obtained in this study, is also comparable with the EEP effect reported by Andersson et al. (2014). Using multiple spacecraft measurements, Andersson et al. (2014) showed that the direct HO_x production due to EEP lead to 90% depletion for a shorter time and 34% depletion for more extended time scales. The effects of the precipitating electrons are also comparable to large but less frequent ozone destruction due to solar proton events (Seppälä, 2004; Verronen et al., 2005).

The SIC model results presented in this study open a way to further study ozone destruction due to PsA electrons using coupled models including transport, such as the WACCM (which includes ion chemistry in the *D* region Verronen et al., 2016) model. By considering the magnitude and the spatial coverage of O_x depletion reported in this study, we anticipate that the atmospheric response to the PsA electron forcing will be significant in the dynamical models as well. As it is also known that PsAs are frequent events with nearly 50% occurrence (Bland et al., 2019), and the HO_x, NO_x, and O_x responses reported in this study did not fully recover within almost 48 hr, there may also be a cumulative atmospheric effect by the precipitating particles.

5. Conclusions

By combining measurements from three spacecraft, we presented statistical PsA electron energy spectrum that includes relativistic and nonrelativistic energies between 30 eV and 1,000 keV. The highest variations of the flux of electrons were observed between 10 and 200 keV, typical for PsA events. The MLT evolution of PsA electrons energy flux does not show any significant trend at any specific energy. However, PsA electrons with higher energies (>30 keV) persisted in the morning hours, while the softer precipitation decayed earlier. The ion chemistry model implemented here showed a wide range of magnitude of O_x depletion between 0% and 78% for short (30 min) to median (120 min) duration of PsA precipitation. The lowest measured fluxes during PsA neither produced HO_x nor depleted ozone, while the highest measured fluxes caused significant ozone depletions both during the forcing and the following night due to the persistent enhancement in the odd hydrogen. The results of this 1-D model raise a number of questions, such as the sensitivity of the atmosphere for the particle forcing, the significance of this depletion in the dynamical model runs, and if observations of change in ozone and associated species during PsA events can be achieved.

Data Availability Statement

MIRACLE ASC quicklook data are available at the website (https://space.fmi.fi/MIRACLE/ASC/?page=keograms), and full-resolution image data can be requested from FMI (kirsti.kauristie@fmi.fi). The entire FAST mission data can be found online (http://sprg.ssl.berkeley.edu/fast/). DMSP particle data are available at CEDAR madrigal database (http://cedar.openmadrigal.org). Event lists, precipitating electrons energy from DMSP, POES, and FAST spacecraft, and SIC model outputs used in this study are available in Tesema et al. (2019).

Acknowledgments
The funding support for F. Tesema and H. Nesse Tyssøy work is provided by the Norwegain Research Council (NRC) under CoE Contract 223252. In addition, the work of N. Partamies is supported by NRC project 287427. The work of C. Smith-Johnsen is supported by the NRC project 263008. The work of Antti Kero is funded by the Tenure Track Project in Radio Science at Sodankylä Geophysical Observatory/University of Oulu. We thank K. Kauristie, S. Mäkinen, J. Mattanen, A. Ketola, and C.-F. Enell for maintaining MIRACLE camera network and data flow. We thank NOAA's SWPC and NCEI (formerly NGDC) for the availability of NOAA POES data.

References

Andersson, M. E., Verronen, P. T., Rodger, C. J., Clilverd, M. A., & Seppälä, A. (2014). Missing driver in the Sun-Earth connection from energetic electron precipitation impacts mesospheric ozone. *Nature Communications*, *5*(1), 5197. https://doi.org/10.1038/ncomms6197

Asikainen, T., & Ruopsa, M. (2016). Solar wind drivers of energetic electron precipitation. *Journal of Geophysical Research: Space Physics*, *121*(3), 2209–2225. https://doi.org/10.1002/2015JA022215

Bland, E. C., Partamies, N., Heino, E., Yukimatu, A. S., & Miyaoka, H. (2019). Energetic electron precipitation occurrence rates determined using the Syowa East SuperDARN radar. *Journal of Geophysical Research: Space Physics*, *124*, 6253–6265. https://doi.org/10.1029/2018JA026437

Carlson, C. W., Pfaff, R. F., & Watzin, J. G. (1998). The Fast Auroral SnapshoT (FAST) Mission. *Geophysical Research Letters*, *25*(12), 2013–2016. https://doi.org/10.1029/98GL01592

Dahlgren, H., Lanchester, B. S., Ivchenko, N., & Whiter, D. K. (2017). Variations in energy, flux, and brightness of pulsating aurora measured at high time resolution. *Annales Geophysicae*, *35*(3), 493–503. https://doi.org/10.5194/angeo-35-493-2017

Eather, R. H., Mende, S. B., & Judge, R. J. R. (1976). Plasma injection at synchronous orbit and spatial and temporal auroral morphology. *Journal of Geophysical Research*, *81*(16), 2805–2824. https://doi.org/10.1029/JA081i016p02805

Evans, D. S., Davidson, G. T., Voss, H. D., Imhof, W. L., Mobilia, J., & Chiu, Y. T. (1987). Interpretation of electron spectra in morningside pulsating aurorae. *Journal of Geophysical Research*, *92*(A11), 12,295. https://doi.org/10.1029/JA092iA11p12295

Evans, D. S., & Greer, M. S. (2000). Polar orbiting environmental satellite space environment monitor—2: Instrument descriptions and archive data documentation. NOAA Tech. Memo., OAR SEC 93, 93, version 1.4, Boulder, Colo., 2004 Jan.

Fukizawa, M., Sakanoi, T., Miyoshi, Y., Hosokawa, K., Shiokawa, K., Katoh, Y., et al. (2018). Electrostatic electron cyclotron harmonic waves as a candidate to cause pulsating auroras. *Geophysical Research Letters*, *45*, 12,661–12,668. https://doi.org/10.1029/2018GL080145

Grono, E., & Donovan, E. (2018). Differentiating diffuse auroras based on phenomenology. *Annales Geophysicae*, *36*(3), 891–898. https://doi.org/10.5194/angeo-36-891-2018

Grono, E., & Donovan, E. (2020). Surveying pulsating auroras. *Annales Geophysicae*, *38*(1), 1–8. https://doi.org/10.5194/angeo-38-1-2020

Hosokawa, K., & Ogawa, P. (2015). Ionospheric variation during pulsating aurora. *Journal of Geophysical Research: Space Physics*, *120*, 5943–5957. https://doi.org/10.1002/2015JA021401

Jaynes, A. N., Lessard, M. R., Rodriguez, J. V., Donovan, E., Loto'Aniu, T. M., & Rychert, K. (2013). Pulsating auroral electron flux modulations in the equatorial magnetosphere. *Journal of Geophysical Research: Space Physics*, *118*, 4884–4894. https://doi.org/10.1002/jgra.50434

Johnstone, A. D. (1978). Pulsating aurora. *Nature*, *274*(5667), 119–126. https://doi.org/10.1038/274119a0

Jones, S. L., Lessard, M. R., Rychert, K., Spanswick, E., & Donovan, E. (2011). Large-scale aspects and temporal evolution of pulsating aurora. *Journal of Geophysical Research*, *116*, A03214. https://doi.org/10.1029/2010JA015840

Jones, S. L., Lessard, M. R., Rychert, K., Spanswick, E., Donovan, E., & Jaynes, A. N. (2013). Persistent, widespread pulsating aurora: A case study. *Journal of Geophysical Research: Space Physics*, *118*, 2998–3006. https://doi.org/10.1002/jgra.50301

Kasahara, S., Miyoshi, Y., Yokota, S., Mitani, T., Kasahara, Y., Matsuda, S., et al. (2018). Pulsating aurora from electron scattering by chorus waves. *Nature*, *554*(7692), 337–340. https://doi.org/10.1038/nature25505

Lessard, M. R. (2012). A review of pulsating aurora. *Aurora Phenomenology Magnetospheric Processes Earth Other Planets*, 55–68. https://doi.org/10.1029/2011GM001187

McEwen, D. J., Yee, E., Whalen, B. A., & Yau, A. W. (1981). Electron energy measurements in pulsating auroras. *Canadian Journal of Physics*, *59*(8), 1106–1115. https://doi.org/10.1139/p81-146

McKay, D., Partamies, N., & Vierinen, J. (2018). Pulsating aurora and cosmic noise absorption associated with growth-phase arcs. *Annales Geophysicae*, *36*(1), 59–69. https://doi.org/10.5194/angeo-36-59-2018

Miyoshi, Y., Oyama, S., Saito, S., Kurita, S., Fujiwara, H., Kataoka, R., et al. (2015). Energetic electron precipitation associated with pulsating aurora: EISCAT and Van Allen Probe observations. *Journal of Geophysical Research: Space Physics*, *120*, 2754–2766. https://doi.org/10.1002/2014JA020690

Miyoshi, Y., Saito, S., Seki, K., Nishiyama, T., Kataoka, R., Asamura, K., et al. (2015). Relation between fine structure of energy spectra for pulsating aurora electrons and frequency spectra of whistler mode chorus waves. *Journal of Geophysical Research: A Space Physics*, *120*, 7728–7736. https://doi.org/10.1002/2015JA021562

Mozer, F. S., Hull, A., Lejosne, S., & Vasko, I. Y. (2018). Reply to Comment by Nishimura Et Al. *Journal of Geophysical Research: Space Physics*, *123*, 2071–2077. https://doi.org/10.1002/2018JA025218

Nesse Tyssøy, H., Sandanger, M. I., Ødegaard, L.-K. G., Stadsnes, J., Aasnes, A., & Zawedde, A. E. (2016). Energetic electron precipitation into the middle atmosphere—Constructing the loss cone fluxes from MEPED POES. *Journal of Geophysical Research: Space Physics*, *121*, 5693–5707. https://doi.org/10.1002/2016JA022752

Nishimura, Y., Bortnik, J., Li, W., Angelopoulos, V., Donovan, E. F., & Spanswick, E. L. (2018). Comment on Pulsating auroras produced by interactions of electrons and time domain structures by Mozer Et Al. *Journal of Geophysical Research: Space Physics*, *123*, 2064–2070. https://doi.org/10.1002/2017JA024844

Nishimura, Y., Bortnik, J., Li, W., Thorne, R. M., Chen, L., Lyons, L. R., et al. (2011). Multievent study of the correlation between pulsating aurora and whistler mode chorus emissions. *Journal of Geophysical Research*, *116*, A11221. https://doi.org/10.1029/2011JA016876

Nishimura, Y., Bortnik, J., Li, W., Thorne, R. M., Lyons, L. R., Angelopoulos, V., et al. (2010). Identifying the driver of pulsating aurora. *Science (80-.).*, *330*(6000), 81–84. https://doi.org/10.1126/science.1193186

Nishimura, Y., Lessard M. R., Katoh Y., Miyoshi Y., Grono E., Partamies N., et al. (2020). Diffuse and Pulsating Aurora. *Space Science Reviews*, *216*(1). https://doi.org/10.1007/s11214-019-0629-3

Ødegaard, L. K. G., Tyssøy, H. N., Søraas, F., Stadsnes, J., & Sandanger, M. I. (2017). Energetic electron precipitation in weak to moderate corotating interaction region-driven storms. *Journal of Geophysical Research: Space Physics*, *122*, 2900–2921. https://doi.org/10.1002/2016JA023096

Oyama, S., Kero A., Rodger C. J., Clilverd M. A., Miyoshi Y., Partamies N., et al. (2017). Energetic electron precipitation and auroral morphology at the substorm recovery phase. *Journal of Geophysical Research: Space Physics*, *122*(6), 6508–6527. https://doi.org/10.1002/2016JA023484

Partamies, N., Whiter, D., Kadokura, A., Kauristie, K., Nesse Tyssøy, H., Massetti, S., et al. (2017). Occurrence and average behavior of pulsating aurora. *Journal of Geophysical Research: Space Physics*, *122*, 5606–5618. https://doi.org/10.1002/2017JA024039

Redmon, R. J., Denig, W. F., Kilcommons, L. M., & Knipp, D. J. (2017). New DMSP database of precipitating auroral electrons and ions. *Journal of Geophysical Research: Space Physics*, *122*, 9056–9067. https://doi.org/10.1002/2016JA023339

Rodger, C. J., Clilverd, M. A., Green, J. C., & Lam, M. M. (2010). Use of POES SEM-2 observations to examine radiation belt dynamics and energetic electron precipitation into the atmosphere. *Journal of Geophysical Research*, *115*, A04202. https://doi.org/10.1029/2008JA014023

Royrvik, O., & Davis, T. N. (1977). Pulsating aurora: Local and global morphology. *Journal of Geophysical Research*, *82*(29), 4720–4740. https://doi.org/10.1029/JA082i029p04720

Rozanov, E., Calisto, M., Egorova, T., Peter, T., & Schmutz, W. (2012). Influence of the precipitating energetic particles on atmospheric chemistry and climate. *Survey of Geophysics*, *33*(3-4), 483–501. https://doi.org/10.1007/s10712-012-9192-0

Samara, M., Michell, R. G., & Redmon, R. J. (2015). Low-altitude satellite measurements of pulsating auroral electrons. *Journal of Geophysical Research: Space Physics*, *120*, 8111–8124. https://doi.org/10.1002/2015JA021292

Sandahl, I. (1984). Pitch angle scattering and particle precipitation in a pulsating aurora—An experimental study. KGI Rept. no. 185. Kiruna, Sweden: Kiruna Geophysical Institute.

Sandahl, I., Eliasson, L., & Lundin, R. (1980). Rocket observations of precipitating electrons over a pulsating aurora. *Geophysical Research Letters*, *7*(5), 309–312. https://doi.org/10.1029/GL007i005p00309

Sandanger, M. I., Ødegaard, L.-K. G., Tyssøy, H. N., Stadsnes, J., Søraas, F., Oksavik, K., & Aarsnes, K. (2015). In flight calibration of NOAA POES proton detectors—Derivation of the MEPED correction factors. *Journal of Geophysical Research: Space Physics*, *120*, 9578–9593. https://doi.org/10.1002/2015JA021388

Sangalli, L., Partamies, N., Syrjäsuo, M., Enell, C. F., Kauristie, K., & Mäkinen, S. (2011). Performance study of the new EMCCD-based all-sky cameras for auroral imaging. *International Journal of Remote Sensing*, *32*(11), 2987–3003. https://doi.org/10.1080/01431161.2010.541505

Sato, N., Wright, D. M., Carlson, C. W., Ebihara, Y., Sato, M., Saemundsson, T., et al. (2004). Generation region of pulsating aurora obtained simultaneously by the FAST satellite and a Syowa-Iceland conjugate pair of observatories. *Journal of Geophysical Research*, *109*, A10201. https://doi.org/10.1029/2004JA010419

Sato, N., Wright, D. M., Ebihara, Y., Sato, M., Murata, Y., Doi, H., et al. (2002). Direct comparison of pulsating aurora observed simultaneously by the FAST satellite and from the ground at Syowa. *Geophysical Research Letters*, *29*(21), 2041. https://doi.org/10.1029/2002GL015615

Seppälä, A., Clilverd, M. A., Beharrell, M. J., Rodger, C. J., Verronen, P. T., Andersson, M. E., & Newnham, D. A. (2015). Substorm induced energetic electron precipitation: Impact on atmospheric chemistry. *Geophysical Research Letters*, *42*, 8172–8176. https://doi.org/10.1002/2015GL065523

Seppälä, A., Lu, H., Clilverd, M. A., & Rodger, C. J. (2013). Geomagnetic activity signatures in wintertime stratosphere wind, temperature, and wave response. *Journal of Geophysical Research: Atmospheres*, *118*, 2169–2183. https://doi.org/10.1002/jgrd.50236

Seppälä, A. (2004). Solar proton events of October November 2003: Ozone depletion in the Northern Hemisphere polar winter as seen by GOMOS/Envisat. *Geophysical Research Letters*, *31*, L19107. https://doi.org/10.1029/2004GL021042

Sinnhuber, M., Nieder, H., & Wieters, N. (2012). Energetic particle precipitation and the chemistry of the mesosphere/lower thermosphere. *Survey of Geophysical*, *33*(6), 1281–1334. https://doi.org/10.1007/s10712-012-9201-3

Smith-Johnsen, C., Marsh, D. R., Orsolini, Y., Nesse Tyssøy, H., Hendrickx, K., Sandanger, M. I., et al. (2018). Nitric oxide response to the April 2010 electron precipitation event: Using WACCM and WACCM-D with and without medium-energy electrons. *Journal of Geophysical Research: Space Physics*, *123*, 5232–5245. https://doi.org/10.1029/2018JA025418

Stenbaek-Nielsen, H. C., & Hallinan, T. J. (1979). Pulsating auroras: Evidence for non collisional thermalization of precipitating electrons. *Journal of Geophysical Research*, *84*(A7), 3257. https://doi.org/10.1029/JA084ia07p03257

Tesema, F., Partamies, N., Tyssøy, H. N., Kero, A., & Johnsen, C. S. (2019). Precipitating electrons energy and SIC model run during pulsating aurora over fennoscandian region. Dataset. https://doi.org/10.6084/m9.figshare.11352065.v1

Tsuchiya, F., Hirai, A., Obara, T., Misawa, H., Kurita, S., Miyoshi, Y., et al. (2018). Energetic electron precipitation associated with pulsating aurora observed by VLF radio propagation during the recovery phase of a substorm on 27 March 2017. *Geophysical Research Letters*, 651–660. https://doi.org/10.1029/2018GL080222

Turunen, E., Kero, A., Verronen, P. T., Miyoshi, Y., Oyama, S. I., & Saito, S. (2016). Mesospheric ozone destruction by high-energy electron precipitation associated with pulsating aurora. *Journal of Geophysical Research: Space Physics*, *121*, 11,852–11,861. https://doi.org/10.1002/2016JD025015

Turunen, E., Verronen, P. T., Seppälä, A., Rodger, C. J., Clilverd, M. A., Tamminen, J., et al. (2009). Impact of different energies of precipitating particles on NOx generation in the middle and upper atmosphere during geomagnetic storms. *Journal of Atmospheric and Solar-Terrestrial Physics*, *71*(10-11), 1176–1189. https://doi.org/10.1016/j.jastp.2008.07.005

Verronen, P. T., Andersson, M. E., Marsh, D. R., Kovács, T., & Plane, J. M. C. (2016). WACCM-D—Whole Atmosphere Community Climate Model with D-region ion chemistry. *Journal Advance Modeling Earth System*, *8*, 954–975. https://doi.org/10.1002/2015MS000592

Verronen, P. T., Seppälä, A., Clilverd, M. A., Rodger, C. J., Kyrölä, E., Enell, C. F., et al. (2005). Diurnal variation of ozone depletion during the October-November 2003 solar proton events. *Journal of Geophysical Research*, *110*, A09S32. https://doi.org/10.1029/2004JA010932

Whalen, B. A., Miller, J. R., & McDiarmid, I. B. (1971). Energetic particle measurements in a pulsating aurora. *Journal of Geophysical Research*, *76*(4), 978–986. https://doi.org/10.1029/JA076i004p00978

Whittaker, I. C., Gamble, R. J., Rodger, C. J., Clilverd, M. A., & Sauvaud, J.-A. (2013). Determining the spectra of radiation belt electron losses: Fitting DEMETER electron flux observations for typical and storm times. *Journal of Geophysical Research: Space Physics*, *118*, 7611–7623. https://doi.org/10.1002/2013JA019228

Yamamoto, T. (1988). On the temporal fluctuations of pulsating auroral luminosity. *Journal of Geophysical Research*, *93*(A2), 897. https://doi.org/10.1029/JA093iA02p00897

Yang, B., Donovan, E., Liang, J., Ruohoniemi, J. M., & Spanswick, E. (2015). Using patchy pulsating aurora to remote sense magnetospheric convection. *Geophysical Research Letters*, *42*, 5083–5089. https://doi.org/10.1002/2015GL064700

Yang, B., Donovan, E., Liang, J., & Spanswick, E. (2017). A statistical study of the motion of pulsating aurora patches: using the THEMIS All-Sky Imager. *Annales Geophysicae*, *35*(2), 217–225. https://doi.org/10.5194/angeo-35-217-2017

Yang, B., Spanswick, E., Liang, J., Grono, E., & Donovan, E. (2019). Responses of different types of pulsating aurora in cosmic noise absorption. *Geophysical Research Letters*, *46*, 5717–5724. https://doi.org/10.1029/2019GL083289